Materials Advances

Accepted Manuscript

This article can be cited before page numbers have been issued, to do this please use: B. S. Tripathy, B. Umapathi, P. Nayak and S. K. Parida, *Mater. Adv.*, 2025, DOI: 10.1039/D5MA00643K.

View Article Online
DOI: 10.1039/D5MA00643K

Comprehensive studies of impedance spectroscopy, Raman, infrared, and ferroelectric properties of $BiFeWO_6$ and application

B. S. Tripathy[a], Balaji Umapathi[b,c], Priyabrata Nayak[b,c], and S. K. Parida[a,*]

[a]Department of Physics, ITER, Siksha O Anusandhan Deemed to be University, Bhubaneswar, India
advanced Materials Technology Department, CSIR-IMMT, Bhubaneswar, India
[c]Academy of Scientific and Innovative Research, Ghaziabad, India

*Corresponding author: santoshparida@soa.ac.in

Abstract

A tetragonal double perovskite $BiFeWO_6$ nanopowders were successfully synthesized via the solid-state reaction technique. Structural characterization using X-ray diffraction (XRD) revealed an average crystallite size of 11.6 *n*m with a lattice strain of 0.06499. Optical properties were investigated through ultraviolet (UV) visible spectroscopy, which determined a bandgap energy of 1.41 eV, highlighting its potential for photovoltaic applications. Raman spectroscopy confirms the presence of all constituent elemental vibrational modes associated with various molecular bonding interactions in the studied material. Dielectric analysis exhibits a Maxwell-Wagner-type polarization effect and promises to be a material with a high dielectric constant and low loss for energy storage devices. The study of impedance plots reveals the negative temperature coefficient of resistance (NTCR) behavior, whereas the electrical modulus study suggests the presence of a non-Debye-type relaxation mechanism. The study of AC conductivity versus frequency and temperature reveals the fact that the conduction mechanism is controlled by the thermally activated charge carriers. Again, semicircular Nyquist and Cole-Cole plots confirm the semiconductor nature and well-supported impedance results. The study of resistance versus temperature shows the NTC thermistor character and became one strong candidate for temperature sensor devices.

Keywords: $BiFeWO_6$; bandgap energy; vibrational modes; non-Debye-type relaxation; NTC thermistor

View Article Online
DOI: 10.1039/D5MA00643K

1. Introduction

The realization of multiferroic material systems has united scientists across the globe with a common interest in exploring phenomena associated with it. The term multiferroic was coined by H. Schmid to define the material system having two or more primary ferroic properties (ferroelectricity, ferromagnetism, ferroelasticity, pyroelectric) in a single phase [1-2]. The term magnetoelectric is a sub-group of multiferroic systems, which includes materials in which electric polarisation can be controlled by varying magnetic fields and vice-versa. This material is characterized by electromagnetic coupling. However, the definition included all the coupling mechanisms associated with charge and spin degrees of freedom [3-4]. Around the 1950s, when ferroelectricity and anti-ferromagnetism were very new physical phenomena. The Soviet Union was the first to try to combine ferroelectric order and magnetic order. Smolenski and Ioffe created magnetic long-range order while retaining the ferroelectric state, in single crystals like Pb $(Fe_{0.5}Nb_{0.5})O_3$ and polycrystalline solid solution like (1-x)$Pb(Fe_{0.66}W_{0.33})$O3-x$Pb(Mg_{0.5}W_{0.5})$ O_3. By the 1960s, only 50 multiferroic systems were known but none of them exhibited properties that are suitable for technological advancement [5]. In 1983, Baryakhtar et al. reported a model that elaborated on how magnetic order induces spontaneous electric polarization by breaking inversion symmetry. In 2000, Spaldin analyzed the idea of Ioffe and Smolenski to explain why ferroelectric and magnetism are against each other in perovskites. This helped scientists to understand the reason why attempts to devise a novel multiferroic failed and encouraged them to take the challenge & this way a new era of multiferroics began [6].

Perovskites are multiferroic materials with structural formula ABX_3 where A is a rare-earth or alkaline cation, B is a transition metal and X symbolizes for halide atom. BX_3 constitutes corner octahedra like that of ReO_3 and A occupies the body center position with coordination number 12. Perovskite oxides have different kinds of electronic properties. $BaTiO_3$ is ferroelectric, $SrRuO_3$ is ferromagnetic, $LaFeO_3$ is weakly ferromagnetic, $BaPb_{1-x}Bi_xO_3$ shows superconducting behavior whereas $LaCoO_3$ shows the insulator-metal transition at the same time many perovskites have metallic conductivity, e.g., ReO_3, A_xWO_3, $LaTiO_3$, $SrVO_3$ & $LaNiO_3$. Interestingly, the strong cation-anion-cation interaction is the cause of metallic conductivity in the ceramic compounds. To enhance the properties in the single perovskite, doubling the unit cell, called as double perovskite materials come in the market.

These materials are invented by doping suitable elements at A and B sites, having general structural formula A'A" B'B" O_6 or A_2B'B" O_6. Suitable elements for B site doping include 3d/4d/5d transition metals, and lanthanides series having small ionic radii. These elements include the most proportion in the periodic table. Thus, providing a wide range of choices for scientists to play with the material and tailor the properties for potential applications. A site can also host two different cations as in A'A" B'B" O_6, named as double-double perovskite. Double perovskites are suitable candidates to replace single perovskites for their performance and stability. In details, they have a greater space to accommodate additional atoms, hence, increasing the compositional space of the perovskite family. A complex atomic environment is created by double perovskites resulting in electronic structures that are absent in single perovskites is another advantage. These perovskites are chemically stable under catalytic conditions such as a wide range of oxidizing and reducing agents, acidic or basic solutions, humidity, heat, light, and CO_2 environments. However, lead toxicity raises a major concern about the commercialization and large-scale application of halide perovskites. Exposure to a small proportion can cause severe damage to the nervous system, and renal system as well as impaired bone calcification. Lead halides having high solubility product constant (K_{SP}) values are easily soluble in water causing damage to ecosystems in the environment. Therefore, scientists are searching for good alternatives to replace lead for the manufacture of perovskites with low toxicity and high performance [7]. Ravi Shankar et. al, have found a long-range anti-ferromagnetic ordering and magnetoelectric coupling in $NaLnNiWO_6$ (Ln= Er, Tm, Lu) [8], Na_3AlF_6, which is a very important material for aluminum processing, Sr_2FeMoO_6 is of greater importance due to its unusual electric and magnetic property arising from the alternation between Mo^V and Fe^{III} ions [9], L. Boudad et. al, reported cubic double perovskites $EuBaFeTiO_6$ and $LaBaFeTiO_6$ with large band gap values 3.53eV and 3.75eV respectively [10], Rutuparna Das et. al, reported anti-ferromagnetic ordering in Y_2CoMnO_6 [11]. Liangdong Chen et. al. reported the application of the double perovskite used as oxygen evolution reaction electrocatalysts and supercapacitors [12]

Ferrite ferromagnetic oxides are known to have high resistivity as well as high permeability. Although ferromagnetic alloys have more than double the value of saturation polarization compared to ferrites, ferrites have advantages in terms of applicability at higher frequency, higher resistivity, low cost, high heat, and corrosion resistance [13-15]. Their chemical stability, biological compatibility, relative ease of preparation, and numerous applications associated with them including mechanical applications [16], magnetic data storage,

View Article Online
DOI: 10.1039/D5MA00643K

microwave absorbers [17-19], sealants, lubricants, coolants [20-21], etc. are the reason of the growing interest about the synthesis of ferrites. The main reason for the increased applicability of ferrites is the ease of detection and manipulation of the application of an external magnetic field. Lithium ferrite, due to high Curie temperature (T_c) and high saturation magnetization (M_s), low magnetic losses, high chemical stability, and high resistivity, is a magnetic material with high technological and scientific interests [22-24].

BFO, or Bismuth ferrite is a multiferroic material that exhibits both ferromagnetic and ferroelectric properties. It is also known for its high value of transition temperatures ($T_c \sim 1100$ K, $T_N \sim 653$ K). Experimental results on BFO came into the picture first time in 1957 [24-26], and its room-temperature ferroelectric property with remnant polarization (P_r) was reported to be more than 50 mC/cm^2 in 1970. Interestingly, in BFO surged in 2003 when Ramesh et al. reported an exceptional increase in remanent polarization ((P_r)), reaching 60 μC/cm², approximately 15 times higher than previously recorded in bulk BFO samples. This breakthrough has since driven further advancements in the material's structural and electronic properties, solidifying its potential in next-generation magnetoelectric devices [26-28]. In recent times, numerous $BiFeO_3$-based multiferroics have been developed by doping suitable elements at either the A-site or B-site or both, which led to a better understanding of the underlying magnetic and electric mechanisms. It is a promising candidate for applications in next-generation storage, information, and spintronics. In traditional ferroelectric materials, the transition metals are characterized by an empty d-shell, known as a d^0 configuration. However, BFO ceramic is different as it does not have any transition metal with an empty d-shell. Instead, it contains Fe^{3+} ions with a d^5 configuration. Interestingly, the ferroelectricity in BFO is not due to these transition metal ions. It is caused by the Bi^{3+} ions (A site cation). An active lone pair of electrons in the valence state in Bi^{3+} ions, in sp^2 hybridized states take part in chemical bonding. The presence of (s^2) lone pair electrons in Bi ions leads to a disruption of local inversion symmetry in BFO. Consequently, the small B-site cation, Fe, minimizes its energy by shifting along the [111] crystallographic directions, influencing the material's structural and electronic properties. This is a unique characteristic of BFO that sets it apart from conventional ferroelectric materials [29].

Tungsten trioxide (WO_3) is indeed a fascinating compound, where its structure is temperature dependent. It is tetragonal at temperatures above 740 °C, orthorhombic from 330 to 740 °C, monoclinic from 17 to 330 °C, triclinic from −50 to 17 °C, and monoclinic again at

View Article Online
DOI: 10.1039/D5MA00643K

temperatures below −50 °C. The most common structure of WO_3 is monoclinic with space group P21/n. The pure compound is an electric insulator, but oxygen-deficient varieties, such as $WO_{2.90} = W_{20}O_{58}$, are dark blue to purple and conduct electricity. These can be prepared by combining the trioxide and the dioxide WO_2 at 1000 °C in a vacuum. Tungsten trioxide is a transition metal oxide known for its n-type semiconductor properties, exhibiting a bandgap ranging from 2.6 to 3.0 eV. This material has garnered significant interest due to its high coloration efficiency, remarkable chemical stability, rapid switching kinetics, and excellent electrochemical activity. These characteristics make WO_3 a promising candidate for applications in electrochromic devices, gas sensors, and energy storage systems [30].

Lastly, WO_3 exhibits fascinating characteristics such as structural and ferroelectric properties, among others. The manifestation of these properties is influenced by the synthesis method employed and the specific conditions under which the experiments are conducted. Notably, WO_3 displays ferroelectric properties at low temperatures (below 230 K) [31]. Consequently, it is anticipated that incorporating a minor quantity of this compound into BFO could lead to intriguing multiferroic properties, including a transition temperature shift. Similar type of work on modified $BiFeWO_6$ is already reported in the literature [32-35]. Interestingly, in this context preliminary structural analysis, microstructure, dielectric, electrical, Raman, infrared, ferroelectric properties of $BiFeWO_6$ ceramics with potential applications is not explored in the single investigation. Therefore, authors have decided to synthesis the same $BiFeWO_6$ ceramic in the solid-state reaction method and investigate all mentioned physical properties in one frame and search possible applications in the field of science and technology. Finally, a comprehensive study on lead-free compound $BiFeWO_6$ is discussed extensively in the next section.

2. Experimental Details

2.1 Raw materials

A cost-effective standard fabrication technique, the high-temperature sintering method, was employed to synthesize single-phase polycrystalline double perovskite $BiFeWO_6$. Analytical reagent (AR) grade raw materials, including Bi_2O_3 (Bismuth oxide), WO_3 (Tungsten oxide), and Fe_2O_3 (Iron(III) oxide), were sourced from M/S Hi-Media Lab with a purity of ≥99%. The raw materials were precisely weighed in stoichiometric ratios using an electronic balance [New

View Article Online
DOI: 10.1039/D5MA00643K

Classic MF: MODEL-ML204/A01], ensuring an accuracy of up to four decimal places. The sample preparation followed the chemical equation detailed below.

$$\mathbf{0.5Bi_2O_3 + 0.5Fe_2O_3 + WO_3 \rightarrow BiFeWO_6}$$

2.2 Synthesis and sintering

The weighed samples were thoroughly mixed through dry grinding using an agate mortar and pestle for 4h for uniform mixing and reduction of powder sample into the nanoscale. The prepared mixture was subjected to calcination in a high-purity alumina crucible for six hours using a high-temperature muffle furnace at 850°C to ensure phase stability. The formation of a stable sample was verified through X-ray diffraction (XRD) analysis using a Rigaku Japan Ultima IV diffractometer (CuKα, $\lambda = 1.540510$ Å). The diffraction patterns were recorded over a broad range of Bragg angles ($20° \leq \theta \leq 80°$) at a scanning speed of 0.2°/min to confirm crystallinity and phase purity. Polyvinyl alcohol is added to calcined powder in 1wt% to make cylindrical pellets using a KBr hydraulic press under a pressure of $4*10^6$ Nm^{-2} of 1-2mm thickness and 10-12mm diameter. The pellet undergoes sintering at 800°C for three hours to enhance its compactness and density, ensuring improved structural integrity and material stability.

2.3 Characterization

The structural characterization was carried out using an X-ray diffractometer (Rigaku Japan Ultima IV, CuKα, $\lambda = 1.540510$ Å) to determine crystallinity and phase purity. Microstructural analysis was conducted using scanning electron microscopy (SEM), with data obtained through an SEM-EDAX system (Model Zeiss EVO 18) to examine surface morphology and elemental composition. The optical properties of the synthesized sample were evaluated using a UV spectrometer (CECIL CE3055, 3000 series), providing insights into its absorption and bandgap characteristics. Additionally, the dielectric properties were investigated using an impedance analyzer, enabling the assessment of its electrical behavior and potential applications in electronic devices. Micro-Raman spectroscopy [lab Ram HR800, Jobin Yvon, wavelength = 488 nm] has been tailored to record the characteristic vibrational modes of the prepared sample. High-temperature dielectric data has been recorded from the LCR analyzer MODEL: N4L PSM, 1735 provided with a frequency range of 1 kHz – 1MHz and temperature range of 25 – 500 °C. The ferroelectric nature of the prepared sample was tested by the polarization versus electric field (P-E) loop tracer (M/S Marine, India) and explored different possibilities for the device applications.

View Article Online
DOI: 10.1039/D5MA00643K

3. Results and discussions

3.1 Sample formation

Goldschmidt's tolerance factor, introduced in 1926, plays a crucial role in predicting the formation, crystal symmetry, and structural stability of the material BMFW. It provides a mathematical framework for assessing the ionic radii compatibility of the constituent elements, ensuring optimal lattice stability and phase formation. This factor can be expressed as:

$$t = \frac{r_{((A+A'))} + r_{(O)}}{\sqrt{2}\left(r_{(B+B')}/_{2} + r_O\right)}$$

where $_{RA}$, $r_{A'}$, r_B, $r_{B'}$, and r_o represent the ionic radii of the A-site cation, A'-site cation, B-site cation, B'-site cation, and the oxygen anion, respectively. The tolerance factor of the studied material has been calculated as 0.96, suggesting a tetragonal structural symmetry [36].

3.2 XRD analysis

X-ray Diffraction (XRD) is a crucial analytical technique for examining the crystalline structure of ceramic materials. By analyzing the angles and intensities of diffracted X-rays, XRD provides essential information about the crystal lattice, phase composition, and crystallite size of ceramics.

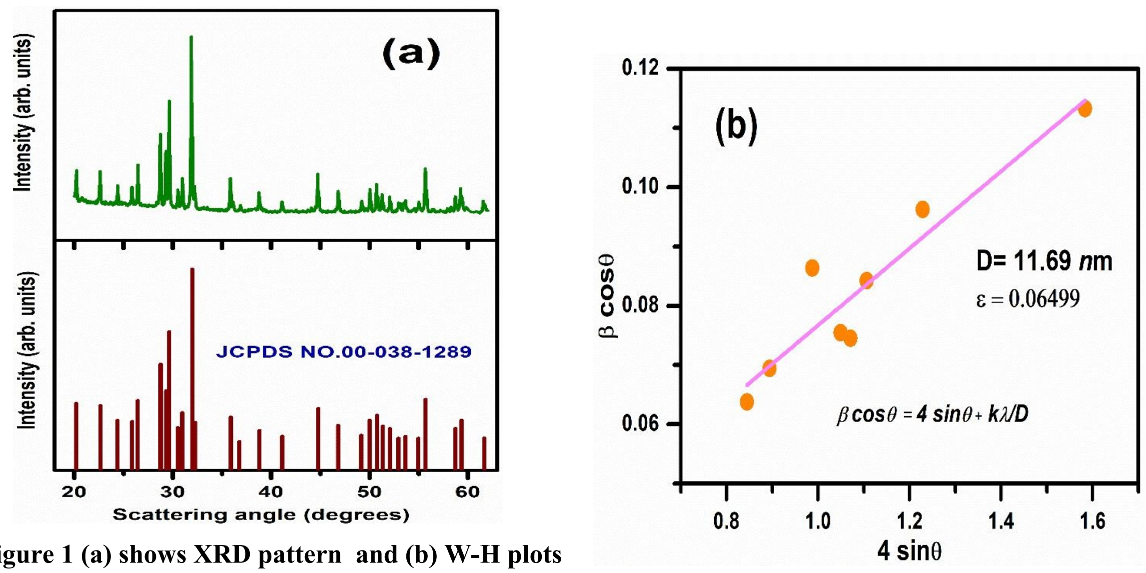

Figure 1 (a) shows XRD pattern and (b) W-H plots of the BFWO ceramic

View Article Online
DOI: 10.1039/D5MA00643K

Figure 1 (a) X-ray diffraction pattern of the $BiFeWO_6$ ceramic at room temperature. The structural analysis was done using X-Pert High-Score software and obtained tetragonal structure (JCPDS: 00-038-1289). The structural lattice parameters are; $a = b = 12.4400$Å, $c = 3.6400$Å and the $\alpha = \beta = \gamma = 90^0$. The average crystallite size (D) and lattice strain (ε) were determined by using Williamson-Hall (W-H) plot as shown in Figure 1 (b). The mathematical relation of W-H method can be written as; $\beta \cos\theta = 4\,\varepsilon \sin\theta + \frac{k\lambda}{D}$, where β represents full width at half-maximum (FWHM) of the reflection, θ is the Bragg angle, λ denotes the X-ray wavelength (~0.154 nm), and k is a dimensionless shape factor, typically assigned a value of ~ 0.89. The calculated average crystallite size was found to be 11.69 *n*m, dislocation density $\sigma = \frac{1}{D^2} = 7.3 \times 10^{-3}\, nm^{-2}$ and lattice micro-strain of 0.06499.

3.3 Microstructural analysis

Field Emission Scanning Electron Microscopy (FESEM) utilizes probing beams that are narrower at both low and high electron energy, enhancing spatial resolution while reducing sample damage. It enables the identification of contamination spots in small areas at electron-accelerating voltages and is compatible with energy-dispersive X-ray spectroscopy. It also allows the application of low kinetic energy electrons closer to the immediate material surface and eliminates the need for conducting coatings on insulating materials [37]. Figure 2 (a) represents the SEM micrograph studied sample. The figure shows the presence of irregularly shaped grains with non-uniform size which depicts that the polycrystalline sample is distorted. However, the grains are distributed uniformly along with well-defined grain boundaries which can be seen from the figure. The high density of the formed sample is confirmed by the closely packed grains leaving negligible voids.

View Article Online
DOI: 10.1039/D5MA00643K

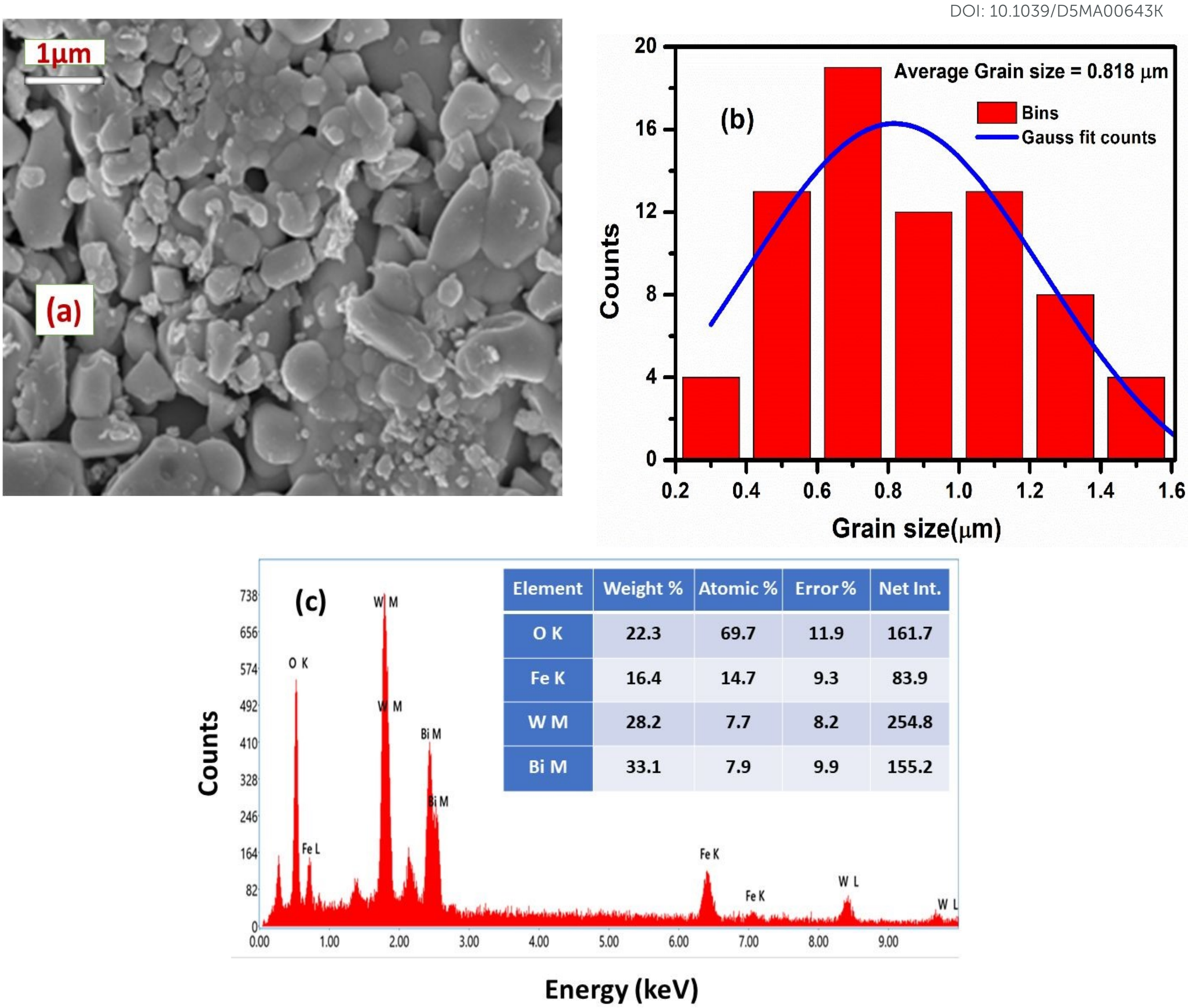

Figure 2 (a) SEM micrograph, (b) Gaussian fitting grain size using ImageJ software, and (c) EDX spectrum confirming the presence of all constituent elements

Figure 2 (b) displays the grain distribution curve, with grain size (in µm) on the x-axis and the number of particles on the y-axis. The ImageJ software was utilized to determine the number of particles and their corresponding grain sizes. The average grain size, determined by fitting the histogram data was found to be 0.818 µm. Grains are highly compact and provide well-defined grain boundaries. The agglomeration ratio i.e., ratio of the grain size to crystallite size is found to be 70, which may be one of the reasons for better electrical conduction process [38]. Figure 2 (c) shows the EDX spectrum of the $BiFeWO_6$ ceramic at room temperature. It is observed that all the constituents (Bi, Fe, W, O) are present in both weight and atomic percentages.

View Article Online
DOI: 10.1039/D5MA00643K

3.4 UV Visible spectroscopy

UV-visible spectroscopy is often used to provide characterization data for various materials including both organic and inorganic chemical substances. When electron transition is induced in a molecule or ion due to the radiation, the material exhibits absorption in the visible or ultra-violet (UV) region. As a result, a change in electronic structure occurs in the material due to absorption of light in the visible or UV region. Inorganic or organic, solid, or liquid groups, such as functional groups can be observed using UV-visible spectroscopy. Depending on the degree of transmittance or absorbance of radiation and sample behavior, UV-visible spectroscopy provides details regarding the bandgap measurements [39].

Figure 3 (a) [inset] show the absorbance spectrum in a range of 200-1100 nm. The sample shows an absorbance peak of 305 nm which is in the UV range, however, the sample absorbs all the visible radiations. Bi-based oxide materials can make use of valence bands O 2p and Bi 6s, have a low bandgap, and absorb more visible radiation [15-16, 40]. The bandgaps in semiconducting materials can either directly allowed, indirectly allowed, directly forbidden, or indirectly forbidden transition depending on the type of material.

In the case of direct(vertical) allowed transition, the energy-dependent absorption coefficient α(E) follows

$$\alpha_{\mathrm{dir}}(E < E_g) = 0$$

$$\text{and} \qquad \alpha_{\mathrm{dir}}(E \geq E_g) \propto (E - E_g)^{1/2}$$

where α_{dir} is the direct optical absorption coefficient, E = hν (photon energy), and E_g is the band gap energy. Such behavior is expected for transitions with negligible changes in electron wave vector k with factors regarding atomic bonding and selection rules. In such a case, the E_g value can be calculated by extrapolating linear least square fit α^2 to 0 in "α^2 versus E_g plot". On the other hand, the indirect transition or non-vertical optical transition involves a photon and at least one phonon to satisfy a conservation of momentum. The transition rate taking place in the case of indirect optical band gap semiconductors is smaller than that in the case of direct band gap semiconductors. The corresponding α(E) follows the relation:

$$\alpha_{\mathrm{dir}}(E < E_g) = 0$$

View Article Online
DOI: 10.1039/D5MA00643K

and $$\alpha_{dir}(E \geq E_g) \propto (E \pm h\nu - E_g)^{1/2},$$

where h$\boldsymbol{\nu}$ represents the energy of the phonon, +h$\boldsymbol{\nu}$ represents the energy of the emitted phonon, and -h$\boldsymbol{\nu}$ is the energy of the absorbed phonon. In most cases, the contribution of h$\boldsymbol{\nu}$ can be neglected.

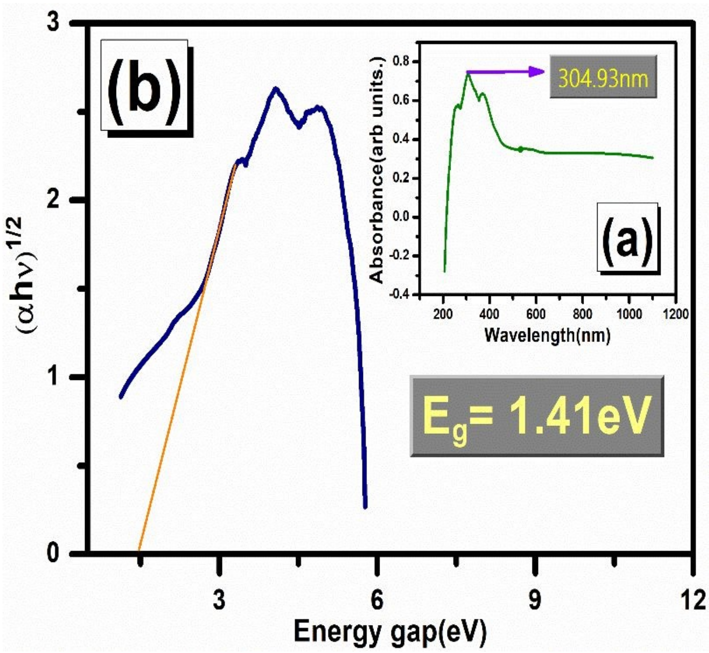

Figure 3 (a) shows absorbance spectrum [inset] and (b) Tauc's plot of the BiFeWO$_6$.

The indirect E_g can be calculated by extrapolating the linear least square fit of $\alpha^{1/2}$ to zero "$\alpha^{1/2}$ versus E" plot as shown in Figure 3 (b). The optical bandgap of the BiFeWO$_6$ sample is calculated following Tauc's mathematical formulation; $\alpha h\nu = A(h\nu - E_g)^{?}$, where A denotes the characteristic parameter, and n represents the exponential term [41]. The parameter γ takes values of 1/2, 2, 3/2, and 3, corresponding to direct allowed, indirect allowed, direct forbidden, and indirect forbidden band transitions, respectively [42]. The value of indirect bandgap energy E_g= 1.41eV in the sample is calculated by extrapolating the linear portion of the plot onto the X-axis corresponding to energy having $(\alpha h\nu)^{1/2}$=0. The calculated bandgap value for the BiFeWO$_6$ is lower than the earlier reported articles, 2.24eV [43], 1.70eV [44], 1.65 [45].

View Article Online
DOI: 10.1039/D5MA00643K

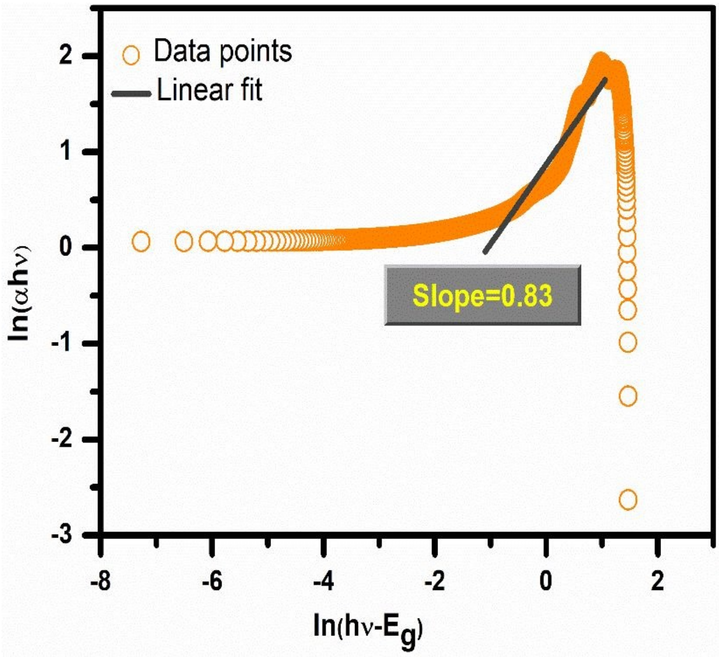

Figure 3 (c) shows the calculation of the *n* value from ln(αhν) versus ln(hν-E_g) of the $BiFeWO_6$

The decrease in bandgap value is due to the oxygen vacancies, which results in positive structural defects. Such sites can capture one or two electrons and act as donor centres. These donor centre levels are located close to the valence band [38]. Tauc's formulation can also be written as: $\ln(\alpha h\nu) = \ln A + \Upsilon \ln(h\nu - E_g)$. The value of *n* is determined from the slope of the plot ln(αhν) versus ln(hν - E_g). The calculated slope of 0.83 deviates from the expected value of 0.5, which corresponds to a direct bandgap transition. This deviation confirms that the sample exhibits an indirect electronic transition [46].

The refractive index (n) is an important optical constant that depends on the wavelength of electromagnetic radiation through dispersion and helps in understanding the optical device application potentiality of any prepared material [47]. Band gap decreases with an increase in refractive index in a semiconducting material, which tells us that these two quantities must be related. S. K. Tripathy et. al. proposed a relation between refractive index and energy band gap, $n = n_o(1+\alpha e^{-\beta E})$, where n_o, α and β are the constants with values 1.73, 1.9017 and 0.539 $(eV)^{-1}$ respectively. Using this formulation, the value of the refractive index for the sample was found to be 3.27 [48]. The refractive index value can be calculated by a model proposed by Kumar and Singh as it includes many different materials including semiconductors materials, halides, insulators, etc. As per the model, the value of the refractive index can be calculated using, $n = K E_g^C$, where K= 3.3668 and C= -0.32234 are constants [24, 25]. So, from the mathematical formulation, the η value was found to be 3.014. The electron polarizability(α') can be calculated

View Article Online
DOI: 10.1039/D5MA00643K

by using the formula, α' =$[\frac{12.41-3\sqrt{E_g-0.365}}{12.41}]\frac{M}{\rho} * 0.395 * 10^{-24}$cm^3, where M is the molecular weight (in g/mol) and ρ is the density of the material (in g/cm^{-3}) [49]. Following the formulation, the value of electron polarizability (α') is found to be 24.84*10^{-24}cm^3. χ^3 is the third-order non-linear optical susceptibility provides detailed information about the strength of chemical bonds between molecules in the synthesized nanocrystalline materials. This quantity can be calculated from first-order susceptibility (χ^1) of ceramics by using; $\chi^1 = \frac{n^2-1}{4\pi}$ and $\chi^3 = A[\chi^1]^4$, where the value of A= 1.7*10^{-10} esu. Using the above formulae, the value of first-order and third-order susceptibility was found to be 0.77 and 6.03*10^{-11}esu respectively [27,28]. Another important parameter is carrier concentration (n_c) in the field of photovoltaics as it influences the doping as well as the oxidation states of crystals [50]. The relation between calculated bandgap (E_g) and carrier concentration (n_c) can be stated as; n_c= $[\frac{\mathbf{E}_g}{2.7924462} * 10^{37}]^{3/2}$[51], which gives the value of n_c as 1.14*10^{55}. This makes the material suitable and potential candidate for optoelectronic applications. We have also calculated the high-frequency dielectric constant (ε_∞) and static dielectric constant (ε_0) using the following mathematical formulation: ε_∞= n^2 and ε_∞=11.26 - 1.42E_g and ε_0 = 18.52 - 3.08E_g [52]. The values of the high-frequency dielectric constant were calculated to be 10.69 (from the refractive index), and 9.2578 (from the energy band gap), and the static dielectric constant value for the prepared sample was found to be 14.177. The oscillator strength value was found to be 2.82eV for the prepared sample, calculated using the relation; oscillator strength = 2E_g [49,53]. The results of different parameters tell us the potentiality of the sample for application in optoelectronic devices. The absorption peak occurs at the UV region of the radiation which implies the material's UV sensing application.

3.5 Raman Study

Raman spectroscopy is a powerful analytical technique used to study vibrational, rotational, and other low-frequency modes in molecules. It is based on the inelastic scattering of light, where incident photons interact with molecular vibrations, leading to a shift in their energy. This technique is widely used in material science, chemistry, biology, and nanotechnology for identifying molecular compositions and structural changes. Raman spectroscopy is highly sensitive to molecular fingerprints, making it essential for non-destructive chemical analysis. It plays a crucial role in studying crystal structures, phase transitions, and even biomedical

View Article Online
DOI: 10.1039/D5MA00643K

diagnostics. Its ability to analyze substances without extensive sample preparation makes it invaluable in scientific and industrial applications.

Figure 4 shows Raman spectrum of the $BiFeWO_6$ ceramic at room temperature. The study of spectrum reveals distinct peaks at 847.9 cm^{-1}, 898.756 cm^{-1}, 1313.997 cm^{-1}, 1507.154 cm^{-1}, 1721.773 cm^{-1}, and 2444.479 cm^{-1}. These spectral features were compared with existing literature to determine their molecular origins. A study of Raman spectra from previously published works suggests that 847.9 cm^{-1} & 898.756 cm^{-1} correspond to Fe-O or W-O stretching vibrations [54], indicating the interaction between iron & tungsten with oxygen, 1313.997 cm^{-1} & 1507.154 cm^{-1} likely associated with Bi-O or Fe-O bond interactions [55], and 1721.773 cm^{-1} & 2444.479 cm^{-1} peaks may be linked to higher-order phonon modes or lattice strain [56].

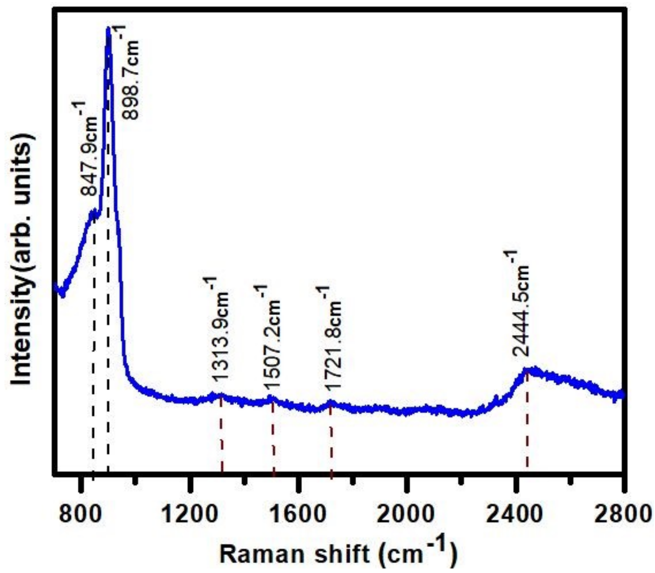

Figure 4 shows the Raman spectrum of the $BiFeWO_6$

3.6 Dielectric study

Figure 5 (a, b) illustrates the variation of dielectric constant (ε_r) and dielectric loss (tanδ) as a function of frequency in the range of 1 kHz to 1 MHz and temperature range of 25°C to 500°C. From Figure 5 (a), we can see that the dielectric values in the low-frequency region are very high in magnitude as well as dispersed and increase with the temperature rise. However, the value of the dielectric constant decreases with the rise in frequency of the applied external electric field and assumes a minimum value at 1MHz even at very high temperatures. The dielectric constant value is determined by the ability of dipolar orientation w.r.t, applied

View Article Online
DOI: 10.1039/D5MA00643K

external field. The types of polarization occurring are classified into four types, electronic, atomic, dipolar, and interfacial. Space charges are the polarizable units for interfacial polarization and with field frequency below 1kHz, the interfacial polarization persists. This is the reason for the high dielectric constant value in lower-frequency regions. Around 1kHz, dipolar polarization comes into the picture which results in the lowering of dielectric constant values at all studied temperatures which is depicted in the plot. Atomic/ionic polarization occurs at around 30-40 kHz, as the increase in magnitude pulls the center of the negatively charged electron cloud away from the nucleus. This further reduces the value of the dielectric constant. At a frequency higher than 100kHz, all other polarization ceases resulting in electronic polarization dominating the polarization phenomenon. Thus, at higher frequencies, the dielectric constant contribution of material is due to electronic polarization solely, which can be understood from the merged plots for all temperatures. At low frequencies, the entire dielectric constant value is due to space polarization. As frequency exceeds a certain value, dipoles lose their ability to align according to the applied field. The contributions of other polarization units decrease, leaving behind only electronic polarization. Thus, the dielectric constant values become invariant and the distinct plots merged at higher frequency regions [58-59]. The loss factor tanδ arises due to the phase difference due to energy loss during the polarization phenomena at various frequencies. The tangent loss appears in a material if the polarization cannot follow with applied electric field. The difference in energy is because total polarization is lagging the applied field. As shown in plot 5 (b), at lower frequency regions, the tangent loss value is high due to the higher values of the dielectric constant. As the frequency increases, the value lowers. The dielectric loss value becomes minimum and invariant as the loss at higher frequencies is only due to electronic polarization, following the same pattern followed by the dielectric constant. The above phenomena were explained by Maxwell-Wagner's two-layer model and Koop's theory [47]. While considering electrical conduction, electrons are more active at grain boundaries in low frequencies whereas at grains during high frequencies. The grain boundaries are characterized by high resistance, hence, more electrical energy loss to facilitate carrier motion when the frequency of the applied field is low. On the other hand, grains offer relatively low resistance, as a result, energy loss is minimized as the applied field frequency increases. Debye's relaxation model also explains the decrease of dielectric constant as well as loss value with an increase in applied field frequency. Since conductivity is frequency-dependent, the accumulation of charge carriers at grain boundaries leads to interfacial or space-charge polarization [58].

DOI: 10.1039/D5MA00643K

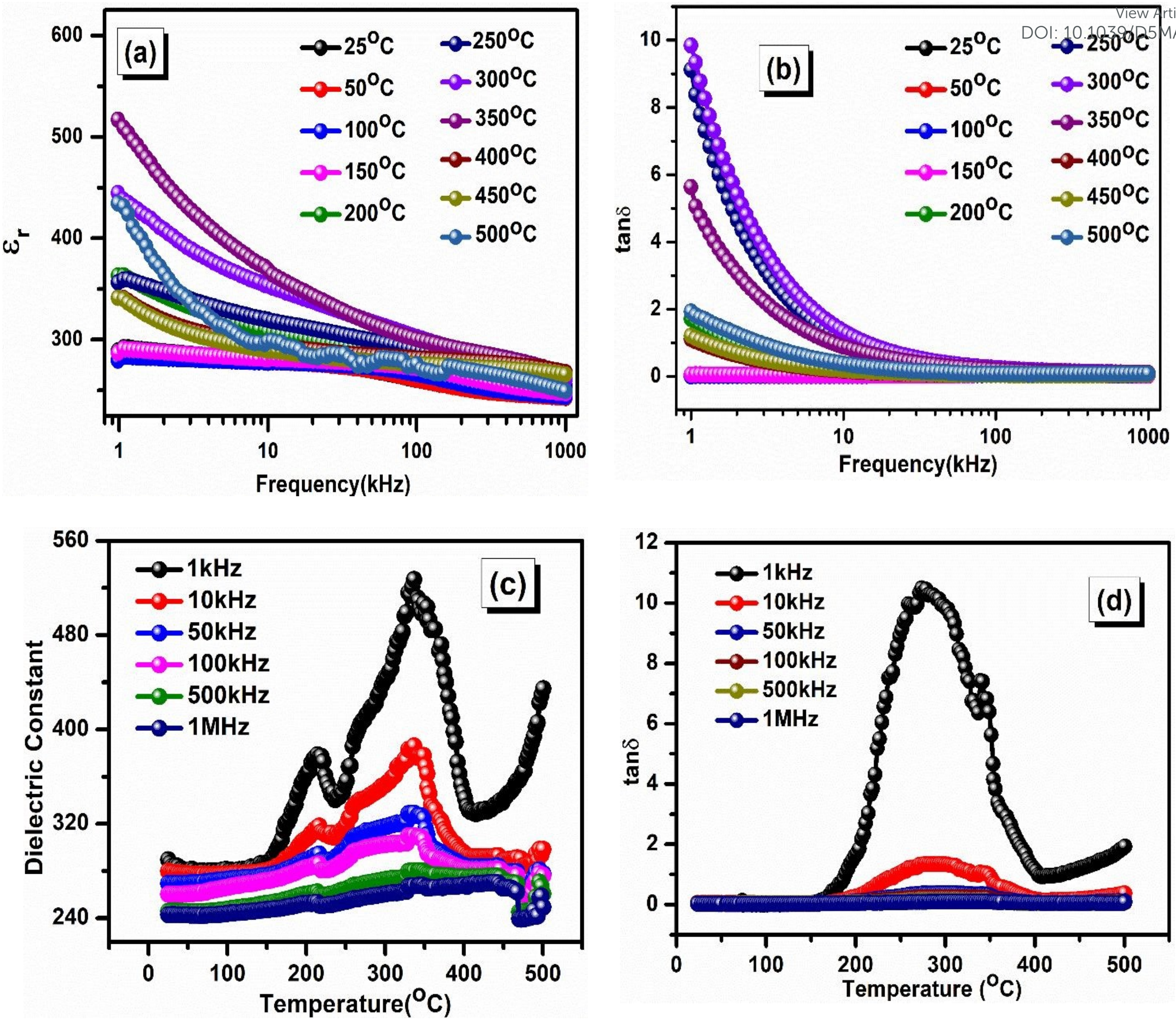

Figure 5 (a, b) shows variation of dielectric constant and tangent loss versus frequency & (c, d) shows variation of dielectric constant and tangent loss versus temperature of the $BiFeWO_6$.

The variation plot of dielectric constant and tangent loss in a temperature range of 25^{O}C to 500^{O}C at a frequency range of 1kHz-1MHz is depicted in Figures 5 (c, d). The dielectric constant increases with rising temperature but decreases as the frequency increases. At lower temperatures, dipoles lack sufficient energy to align with the applied electric field, resulting in a lower dielectric constant [59]. In Figure 5 (c), around the reported Neel's temperature (~370^{0}C), an anomaly can be observed in the permittivity value [60]. The peaks of the dielectric constant value are due to the change in state of electric dipole ordering probably due to the presence of anti-ferromagnetic transition or magnetoelectric effect in the sample [61]. The Landau- Devonshire theory of phase transition describes such an anomaly in magnetoelectric systems which is an effect of vanishing magnetic order on electric order [62]. The plot corresponding to 1kHz frequency shows the maximum value of dielectric constant around 350^{0}C. As the frequency increases, the ε_{max} value decreases due to the electron-phonon

View Article Online
DOI: 10.1039/D5MA00643K

interactions [63]. Above 390^{0}C, the increase in the value of the dielectric constant can be attributed to the thermally activated transport process and the presence of space charges. The space charge contribution is the result of oxygen vacancies created during the sintering of sample pellets at high temperatures [64]. Due to the oxygen vacancies, the valency state of Fe^{3+} changes to Fe^{2+}. Besides the oxygen vacancies, the rise in ε_r value also effects of electron hopping in the direction of the applied electric field, between Fe^{3+} and Fe^{2+} octahedral sites [65]. Above 390^{0}C, an increase in the value of ε_r can be seen which is due to the dipolar contribution of $BiFeO_3$ ferroelectric. Figure d shows the temperature dependence of tanδ in a frequency range of 1kHz to 1MHz. The plots follow a similar pattern as that of ε_r. In low-temperature regions, the plots are merged into one. But, with an increase in temperature, tanδ value increases rapidly following an increase in ε_r values. For temperature values above 300^{0}C, the values decrease due to the scattering of thermally activated charge carriers and the oxygen point defects. For an ideal case, the material should possess high resistance and low dielectric loss. The vacancies generated during high-temperature sintering may lead to the release of single or double-ionized oxygen vacancies, accompanied by the liberation of one or two electrons, respectively. Dielectric relaxation is influenced by dipoles, while oxygen vacancies extend beyond a single unit cell, impacting the entire material and contributing to an increase in ionic conductivity.

3.7 Impedance study

Impedance spectroscopy is related to the permittivity and distinguishes between the conducting and non-conducting regions of the sample. At shorter time scales, electrical spectroscopy serves as an effective tool for analyzing both electronic and ionic conduction properties. The frequency-dependent permittivity spectrum can be measured from these relaxation times. Permittivity reduces the dielectric constant [66].

Mathematical tools that helped electrical impedance spectroscopy are as:

$$\mathbf{Z^* = Z' + jZ''}$$

$$\mathbf{Z' = \frac{R}{1 + (\omega\tau)^2}}$$

$$\mathbf{Z'' = \frac{-\omega R\tau}{1 + (\omega\tau)^2}}$$

View Article Online
DOI: 10.1039/D5MA00643K

Where Z^* represents the complex impedance, with Z' as its real part and Z" as its imaginary part. R denotes resistance, j is the imaginary unit $\sqrt{-1}$, while ω and τ correspond to angular frequency and relaxation time, respectively [67]. Figure 6 (a, b) shows the frequency dependence plots of Z' and Z" complex impedances at selected temperatures. As can be seen from the plot, the value of both Z' and Z" decreases with increase in frequency and temperature. The Z' plots at higher frequencies merge owing release of space charges resulting in a reduction of barrier properties in the sample at higher frequencies [67].

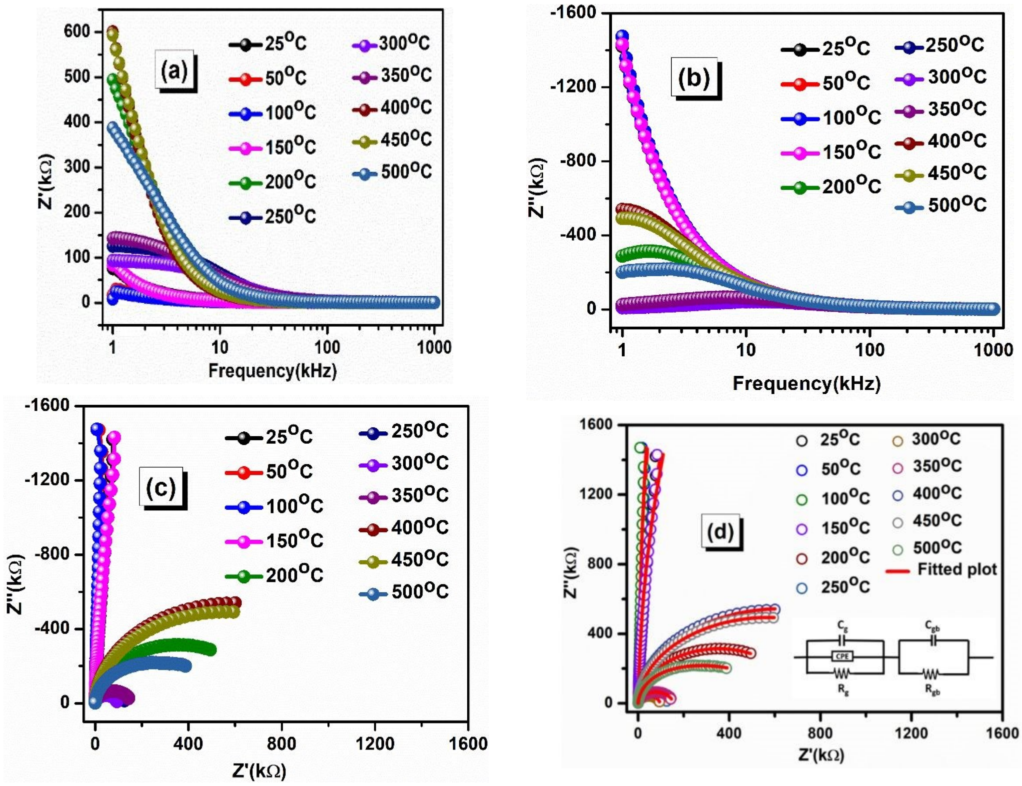

Figure 6 (a) Z' versus frequency, (b) Z" vs frequency and (c) Nyquist plots and (d) Fitted Nyquist plots of the $BiFeWO_6$

The increase in conductivity observed in the sample with rising temperature and frequency is associated with a single relaxation phenomenon. This tells us about the negative temperature coefficient of the resistance behaviour of the sample. Negative temperature coefficient of resistance (NTCR) behaviour is a defining characteristic of semiconducting materials, indicating the dielectric nature of the sample [68]. The spectrum loss of Z" in Figure 6 (b) varies with frequency, as evidenced by the presence of a distinct peak. The shift of the relaxation process to higher frequency regions with increasing temperature indicates its temperature dependence. Asymmetrically broadened peaks observed over time suggest the presence of multiple relaxation mechanisms. At lower temperatures, relaxation is primarily influenced by electrons and immobile ions, whereas at higher temperatures, oxygen vacancies and defects

View Article Online
DOI: 10.1039/D5MA00643K

play a dominant role. The conductivity in the sample arises from electron hopping and oxygen vacancies generated during high-temperature sintering of the pellets, facilitating charge transport among localized sites. Figure 6 (c, d) illustrates Nyquist plots and fitted Nyquist plots of the sample at some selected temperatures, offering insights into the roles of grains and grain boundaries in its conduction mechanism. At lower frequencies, conduction is primarily governed by grain boundaries, whereas at higher temperatures, grains play a dominant role. The presence of semicircular arcs in the Nyquist plot further confirms the semiconducting nature of the sample. This equivalent circuit is composed of a suitable combination of resistance (R) and capacitance (C) connected in parallel for each arc. In addition, a constant phase element (Q) is coupled with the RC circuit, providing information about the depression angle, i.e., a departure from ideal Debye-type relaxation behavior. To provide a detailed view of the actual contribution of the grain and grain boundary, the Nyquist data were fitted and simulated with an equivalent electrical circuit, i.e., (CQR)(CR) at some selected temperatures. In this study, the fitted parameters obtained from fitting Nyquist data using the ZSIMPWIN version 2.0 software code are bulk (grain) capacitance (Cg), constant phase factor (Q), bulk resistance (Rg), grain boundary resistance (Rgb), capacitance (Cgb) and frequency power (n), and these are listed in Table 1. It is observed that the grain boundary effect is suppressed and grain resistance becomes effective at higher temperatures. The resistance at the grain boundary decreases from 8.943 x10^9 Ωcm^2 at 25°C to 3.547x10^5 Ωcm^2 at 500°C. This confirms NTCR character of the studied sample [69].

Table-1 represents fitting parameters from Nyquist plots after coupled with equivalent circuit (CQR)(CR) using the ZSIMPWIN version 2.0 software of the $BiFeWO_6$

Temperature	C_g (F/cm^2)	Q (S-sec^2/cm^2)	R_g (Ω.cm^2)	Frequency Exponent (n)	R_{gb} (Ω.cm^2)	C_{gb} (F/cm^2)
25^{0}C	4.9E-10 (Expt.) 4.9E-10 (Fitting)	2.714E-10 (Expt.) 2.717E-6 (Fitting)	8.943E9 (Expt.) 1.878E16 (Fitting)	21.06	2.388E7 (Expt.) 2.387E7 (Fitting)	1.122E-10 (Expt.) 1.122E-10 (Fitting)
50^{0}C	6.205E-10 (Expt.) 6.205E-10 (Fitting)	0.002798 (Expt.) 2.8E-5 (Fitting)	1.427E10 (Expt.) 3.741E11 (Fitting)	39.46	6.174E7 (Expt.) 6.172E7 (Fitting)	1.089E-10 (Expt.) 1.089E-10 (Fitting)
100^{0}C	6.411E-10 (Expt.) 6.412E-10 (Fitting)	5.22E-5 (Expt.) 5.221E-5 (Fitting)	1.048E11 (Expt.) 7.163E11 (Fitting)	59.03	6.739E7 (Expt.) 6.737E7 (Fitting)	1.084E-10 (Expt.) 1.084E-10 (Fitting)

View Article Online
DOI: 10.1039/D5MA00643K

150⁰C	4.972E-10 (Expt.) 4.972E-10 (Fitting)	4.842E-8 (Expt.) 4.842E-6 (Fitting)	1.527E11 (Expt.) 3.523E15 (Fitting)	30.48	1.986E7 (Expt.) 1.986E7 (Fitting)	1.11E-10 (Expt.) 1.11E-10 (Fitting)
200⁰C	2.975E-19 (Expt.) 2.975E-19 (Fitting)	2.949E-10 (Expt.) 2.95E-10 (Fitting)	6.017E5 (Expt.) 6.016E5 (Fitting)	1.356	1.012E5 (Expt.) 1.012E5 (Fitting)	4.621E-10 (Expt.) 4.621E-10 (Fitting)
250⁰C	7.706E-11 (Expt.) 7.706E-11 (Fitting)	1.843E-9 (Expt.) 1.843E-10 (Fitting)	1.285E5 (Expt.) 1.285E5 (Fitting)	1.108	236.7 (Expt.) 236.8 (Fitting)	1.633E-9 (Expt.) 1.633E-9 (Fitting)
300⁰C	7.226E-11 (Expt.) 7.24E-11 (Fitting)	4.043E-10 (Expt.) 4.051E-10 (Fitting)	9.554E4 (Expt.) 9.554E4 (Fitting)	9.018	107.1 (Expt.) 107.1 (Fitting)	4.174E-9 (Expt.) 4.131E-9 (Fitting)
350⁰C	8.682E-11 (Expt.) 8.684E-11 (Fitting)	7.508E-10 (Expt.) 7.515E-10 (Fitting)	1.414E5 (Expt.) 1.414E5 (Fitting)	1.746	1.413E4 (Expt.) 1.413E4 (Fitting))	6.576E-10 (Expt.) 6.577E-10 (Fitting)
400⁰C	4.821E-14 (Expt.) 1.528E-16 (Fitting)	2.835E-11 (Expt.) 2.835E-10 (Fitting)	9.344E5 (Expt.) 9.344E5 (Fitting)	2.83	2.799E5 (Expt.) 2.798E5 (Fitting)	2.744E-10 (Expt.) 2.744E-10 (Fitting)
450⁰C	8.318E-19 (Expt.) 8.307E-19 (Fitting)	2.573E-10 (Expt.) 2.576E-10 (Fitting)	3.926E5 (Expt.) 3.921E5 (Fitting)	2.461	6.974E5 (Expt.) 6.978E5 (Fitting))	2.741E-10 (Expt.) 2.738E-10 (Fitting)
500⁰C	2.64E-18 (Expt.) 2.419E-18 (Fitting)	1.088E-8 (Expt.) 1.088E-9 (Fitting)	3.547E5 (Expt.) 3.547E5 (Fitting)	2.78	2.292E5 (Expt.) 2.292E5 (Fitting)	1.663E-10 (Expt.) 1.663E-10 (Fitting)

3.8 Modulus Study

Different phenomena e.g., bulk properties, conduction effect, relaxation time, effect of grain boundaries, electrode polarization, and electric transport process can be understood from the electric modulus spectroscopy. It also helps in separating spectral components having different capacitances but the same resistances. Mathematical tools that were useful in calculating complex modulus(M*), real modulus(M') and complex modulus(M") are as follows:

$$\mathbf{M^* = M' + jM''},$$

$$\mathbf{M' = B\frac{(\omega\tau)^2}{1+(\omega\tau)^2}}, \qquad \text{and}$$

$$\mathbf{M'' = B\frac{\omega\tau}{1+(\omega\tau)^2}}$$

DOI: 10.1039/D5MA00643K

where, j= $(-1)^{1/2}$; τ= relaxation time and ω= angular frequency. The bulk and grain boundary effects, along with the inhomogeneous nature of the polycrystalline sample, can be analyzed using the equations, which could not be fully explored through impedance spectroscopy. Additionally, modulation formulations play a crucial role in suppressing electrode effects, ensuring a more accurate characterization of the sample's electrical properties [70]. Figure 7 (a) represents the frequency versus real modulus (M') graph in a frequency range of 1kHz-1MHz at some selected temperatures. The 25^0C- 150 ^{0}C plots show that at low-frequency regions, M' values are at peak than rest temperature plots. The plots for 250 ^{0}C - 350 ^{0}C have modulus values that are nearly equal to zero at low-frequency regions. In low-frequency regions, the modulus value dropping to zero may be due to the absence or low electrode polarization. The merging of the plots and the attainment of high M' values in higher frequency regions can be attributed to low-mobility charge carriers, coupled with the absence of a restoring force under the induced electric field [70]. The M" as a function of frequency for selected temperatures is plotted in Figure 7 (b). M" values increase with the increase in frequencies and reach a maximum value of M''_{max}. The peaks for M''_{max} shifts towards a higher frequency region depict the presence of relaxation phenomenon occurring in the sample [71]. The capacitance is inversely proportional to the height of the peak. The plots illustrate the transition from long-range to short-range charge carrier mobility. The region to the left of the peaks corresponds to long-range mobile charge carriers, while beyond M''_{max}, ions become confined within potential wells due to the short-range mobility of charge carriers. Study of M" confirms the occurrence of non-Debye relaxation behaviour concluded from the appearance of asymmetrically broadened peak curves unlike in ideal Debye type.

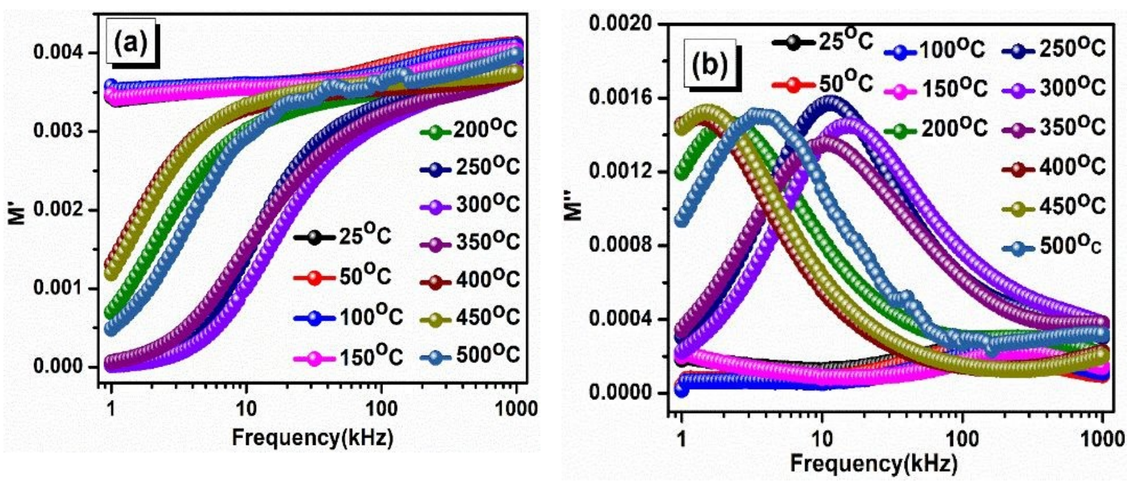

View Article Online
DOI: 10.1039/D5MA00643K

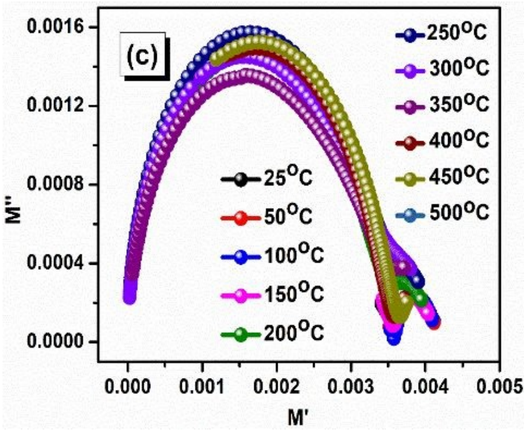

Figure 7 (a) M' versus frequency, (b) M'' versus frequency, and (c) Cole- Cole plots of the $BiFeWO_6$

The appearance of an arcs at a frequency in the Cole-Cole plots Figure 7 (c) signifies that the sample material has a single phase. The change in nature of curves with a temperature change is due to a change in capacitances tells us about the temperature dependence of capacitance. Some curves in the Cole-Cole plots have their centres lying below the real modulus axis again providing evidence of the presence of a non-Debye-type relaxation process in the material. The intercept of large curves on the real modulus axis gives the value of capacitance contribution from grains whereas the intercepts of the smaller curves give the grain boundary capacitance contribution. These semicircular arcs are also an indication of the semiconducting nature of the sample [72].

3.9 AC conductivity study

The ac conductivity of a sample can be calculated from dielectric data using the relation: $\sigma_{ac}=\omega\varepsilon_r\varepsilon_0\tan\delta$, where ω is the angular frequency, ε_0 is the permittivity of free space (approximately 8.854×10^{-12} F/m), ε_r is the relative permittivity (or dielectric constant), and tanδ is the dielectric loss [73]. At low frequencies, the frequency-dependent conductivity plot stabilizes, forming a plateau that signifies DC conductivity, resulting from the random dispersion of ionic charge carriers through active hopping. On the other hand, in the high-frequency region, the plot becomes dispersive due to an increase in conductivity. This increase in conductivity at high frequencies is indicative of the dynamic nature of charge transfer processes in the material. In essence, these studies allow us to understand the complex interplay between charge carriers, their transfer processes, and how these factors influence the overall conductivity of the material. The frequency dependence of the conductivity of a sample can indeed be studied using Jonscher's universal power law, which is given by the equation: $\sigma_{ac}=\sigma_{dc}+A\omega^n$, where σ_{ac} is the ac conductivity, σ_{dc} is the dc conductivity, A is the polarizability

View Article Online
DOI: 10.1039/D5MA00643K

strength, ω is the angular frequency, and *n* is the frequency exponent which ranges from 0 to 2 [74].

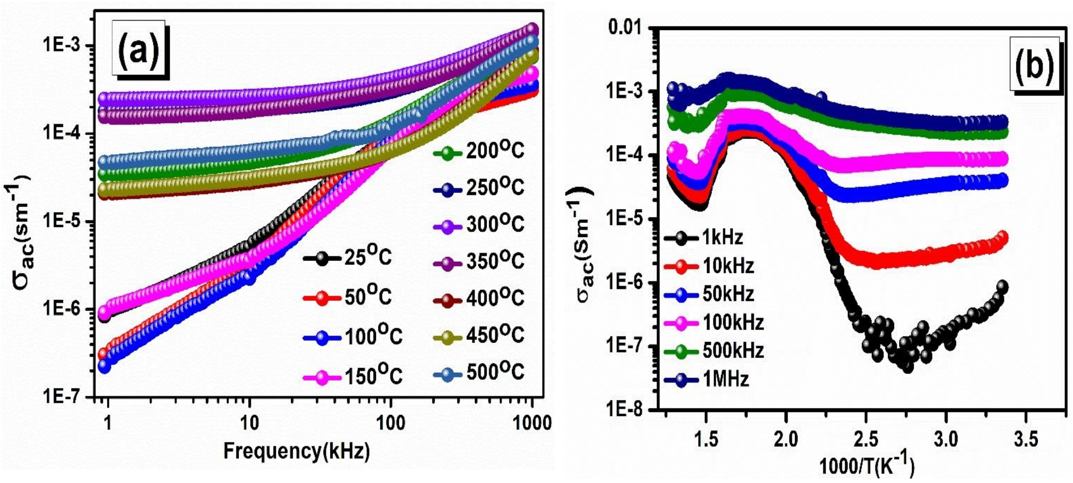

Figure 8 (a) σ_{ac} versus frequency and (b) σ_{ac} versus 1000/T plots of the $BiFeWO_6$

The fitting data are recorded in the Table-2. This law is widely used in the study of dielectric materials and provides valuable insights into the behaviour of charge carriers in the material. The parameters A and n are typically determined through experimental measurements and can provide information about the material's response to different frequencies.

Table-2 represents evaluated values of the σ_{dc} , n, A, and R^2 of the $BiFeWO_6$

View Article Online
DOI: 10.1039/D5MA00643K

Temperature(°C)	σ_{dc} (Sm^{-1})	*n*	A	R^2
25	-1.0715E-5	0.7778	1.10156E-8	0.84933
50	-1.3135E-5	0.77356	1.16045E-8	0.80118
100	-1.8911E-5	0.77889	1.27098E-8	0.82463
150	-1.1215E-5	0.76152	1.50523E-8	0.98018
200	2.6256E-5	0.80084	1.21889E-8	0.99083
250	1.6592E-4	0.81095	1.35699E-8	0.99628
300	2.3386E-4	0.81115	1.65958E-8	0.99929
350	1.6835E-4	0.97778	1.77533E-9	0.99788
400	2.6881E-5	1.42847	2.2962E-12	0.9996
450	3.0873E-5	1.46646	1.1702E-12	0.9988
500	4.9793E-5	1.11066	2.3723E-10	0.9979

Table-3 represents evaluated values of activation energy and corresponding frequency of the $BiFeWO_6$

Sl No.	Frequency	Activation energy (E_a) (meV)
1	1 kHz	374.81
2	10 kHz	291.69
3	50 kHz	188.28
4	100 kHz	135.63
5	500 kHz	66.47
6	1 MHz	49.17

Figure 8 (a, b) illustrate the variation of ac conductivity as a function of frequency and 10^3/T (K^{-1}) at some selected frequencies. As shown in Figure 8 (a), AC conductivity increases with both frequency and temperature, where the lower portion of the conductivity plot contributes to DC conductivity. Examining the temperature dependence of AC conductivity provides

View Article Online
DOI: 10.1039/D5MA00643K

insights into the total real charge carriers within the sample. The rise in AC conductivity with increasing temperature confirms the NTCR characteristic, indicating semiconducting behavior. The activation energy of the ceramic compound can be determined using the Arrhenius equation: $\sigma = \sigma_0 * e^{\frac{-E_a}{k_B T}}$, Where k_B represents the Boltzmann constant, and E_a denotes the activation energy [74]. The computed activation energy values at different frequencies are presented in Table 3. The observed decrease in activation energy with increasing frequency supports the presence of a thermally activated relaxation mechanism in the sample.

3.10 Thermistor characteristics

In previous sections, we explored the dielectric, optical, conducting as well as transport properties of the ceramic sample. Impedance characteristics show the presence of both grain and grain boundary effects as well as its NTCR behaviour. Authors have then with the interest of exploring the industrial application, studied thermistor characteristics of the ceramic sample. Thermistors are of two types: positive temperature coefficient (PTC) and negative temperature coefficient NTC. In PTC thermistors, resistance increases with the rise in temperature, while in NTC thermistors, resistance decreases with the rise in temperature. Figures 9 (a) illustrates variation of the resistance with temperature. The decrease in resistance with increasing temperature confirms the NTC thermistor nature upto 375^0C, PTC thermistor up to 425^0C and then again NTC thermistor up to 500^0C. Consequently, $BiFeWO_6$ ceramic emerges as a promising candidate of a non-toxic thermistor suitable for various industrial applications.

(a) Activation energy

Figure 9 (b) illustrates the variations in temperature-dependent activation energy (Ea). The activation energy is determined using the mathematical relation presented as: $E_a = k_B \times \beta$, where k_B denotes the Boltzmann constant, and β represents the thermistor constant. The activation energy curve exhibits a similar trend when compared to the behavior of the thermistor constant

(b) Thermistor constant (β)

Figure 9 (c) shows the variation of the thermistor constant with temperature. The thermistor constant can be calculated by using empirical relation: $\beta = \ln\left(\frac{R_1}{R_2}\right) / \ln\left(\frac{1}{T_1} - \frac{1}{T_2}\right)$, where R_1

View Article Online
DOI: 10.1039/D5MA00643K

and R_2 as initial and final resistances at temperatures T_1 and T_2 respectively. The value of the thermistor constant fall in the good range for NTC thermistor applications [75].

(c) Sensitivity factor (α)

Figure 9 (d) shows the variation of the sensitivity factor versus temperature. The sensitivity factor represents a crucial parameter of thermistors, quantifying the rate at which resistance varies in response to temperature fluctuations. The sensitivity factor is calculated using the following mathematical relation: $\alpha = \left(\frac{-\beta}{T^2}\right) \times 100$, where α is the sensitivity factor, β is the thermistor constant and T is the temperature in K [75].

.

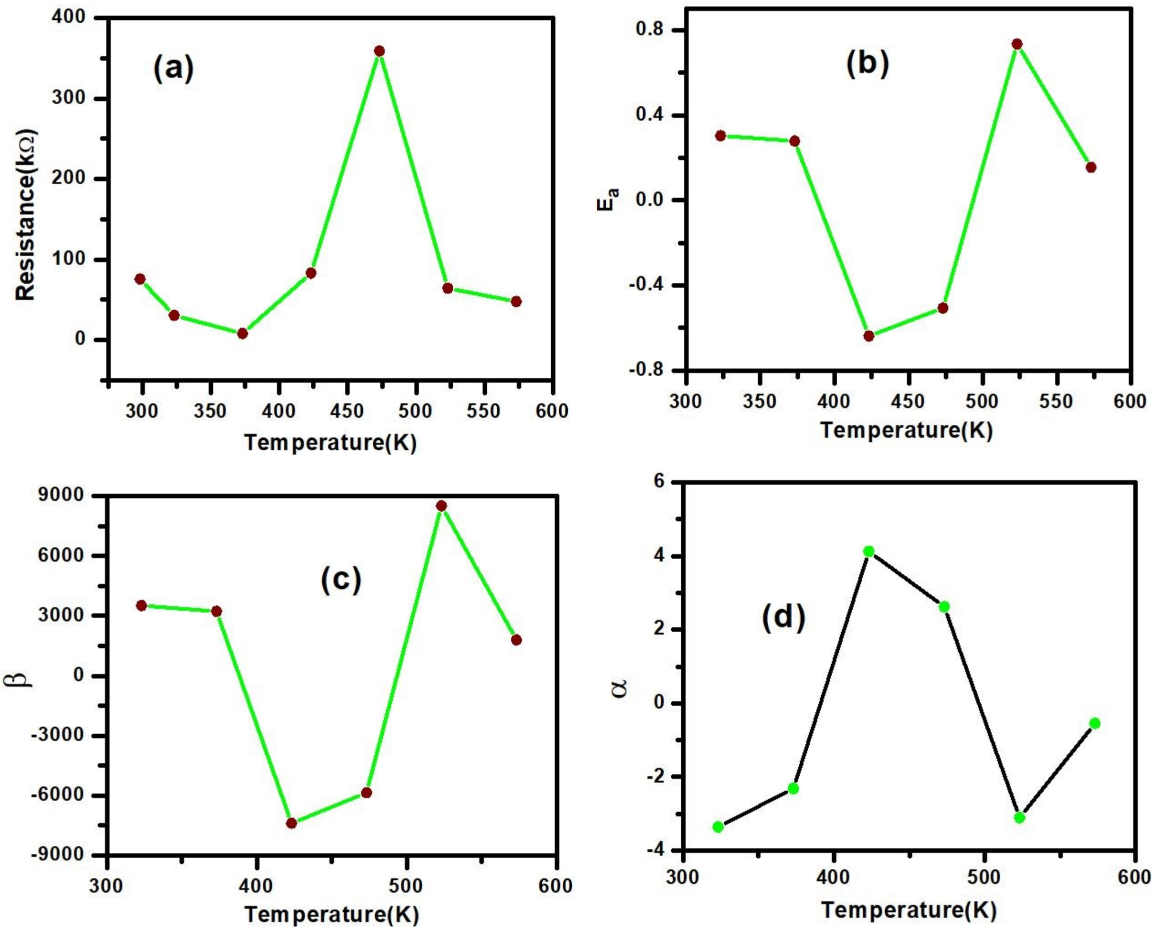

Figure 9 (a) shows variation of resistance with temperature, (b) activation energy versus temperature, (c) thermistor constant versus temperature and (d) sensitivity factor versus temperature of the $BiFeWO_6$

View Article Online
DOI: 10.1039/D5MA00643K

The mathematical relationship reveals that the parameter α exhibits direct proportionality to β while demonstrating an inverse dependence on the square of temperature. A higher α value corresponds to increased mobility of charge carriers compared to lower α magnitudes. The figure illustrates the variation of the sensitivity factor with temperature, highlighting its nonlinear inverse correlation with the square of absolute temperature. The presence of half-filled transition metal cations at the B-site, forming an octahedral coordination with oxygen, plays a pivotal role in enhancing material properties. This structural configuration significantly contributes to improved findings, thereby broadening the scope of thermistor-related applications [76].

3.11 Ferroelectric properties

P-E loop (Polarization-Electric field) is a graphical representation of the hysteresis behaviour of ferroelectric materials. It plots polarization (P) against the electric field (E) applied to a material, demonstrating how the material retains its polarization even after the external field is removed. P-E loops are widely used in research and applications such as ferroelectric memory devices, capacitors, and sensors. Since we are working with ferroelectric materials, analyzing the P-E loop can provide valuable insights into their electrical properties. Lead-free relaxor ferroelectrics exhibit advantageous properties, including low remanent polarization, high maximum polarization, enhanced breakdown strength, and excellent thermal stability. Extensive research has been conducted on dielectric energy storage materials utilizing relaxor ferroelectrics, particularly those based on $SrTiO_3$ (ST), $BaTiO_3$ (BT), $NaNbO_3$ (NN), and $Na_{0.5}Bi_{0.5}TiO_3$ (NBT) ceramics [77].

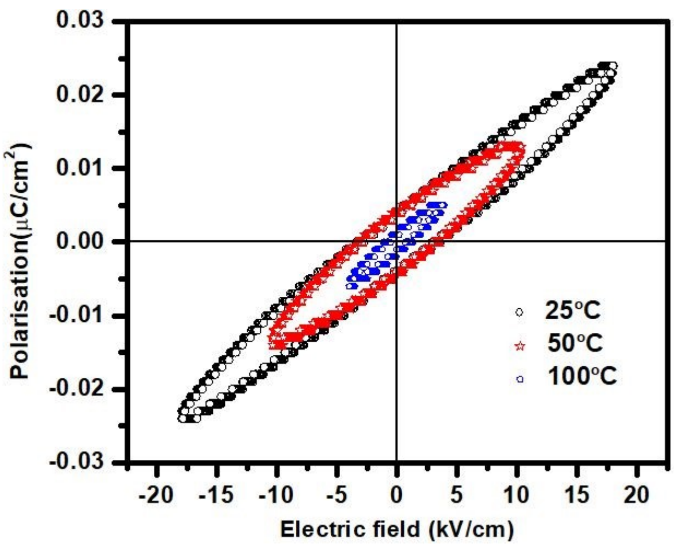

View Article Online
DOI: 10.1039/D5MA00643K

Figure 10 shows the P-E hysteresis loop of the $BiFeWO_6$

Figure 10 shows the PE loops at three different temperatures of 25^0C, 50^0C, and 100^0C. The plot shows maximum polarisation values of 0.024μC/cm^2 at 25^0C which gradually decreases to 0.013μC/cm^2 at 50^0C and 0.005μC/cm^2 at 100^0C. Also, it can be observed that with an increase in temperature values the values of remnant polarisation and coercive field decrease.

The decrease in coercive field value with increasing temperature, while maintaining constant frequency, signifies a reduction in the material's ability to retain polarization under an applied electric field. This phenomenon is primarily attributed to the thermal activation of dipoles, which disrupts their alignment and facilitates easier polarization switching. Additionally, as the material approaches its Curie temperature, its ferroelectric properties weaken, leading to a significant drop in the coercive field. Reduced domain wall pinning at elevated temperatures further contributes to this effect, as defects and lattice distortions that typically hinder domain movement become less restrictive. Moreover, structural softening at higher temperatures lowers the energy barrier required for domain switching, making polarization reversal more efficient. These temperature-dependent variations in the coercive field are crucial for applications such as ferroelectric memory devices, capacitors, and sensors, where thermal stability plays a vital role in performance optimization [78-79]. An increase in temperature while keeping frequency constant typically leads to a decrease in remnant polarization. This occurs because thermal energy disrupts the alignment of dipoles within the ferroelectric material, reducing its ability to retain polarization after the external electric field is removed. Additionally, as the temperature rises, the material may approach its Curie temperature, beyond which it loses its ferroelectric properties and transitions into a paraelectric phase. This phenomenon is crucial in applications such as pyroelectric sensors and ferroelectric memory devices, where temperature stability is essential [80].

4. Conclusion

$BiFeWO_6$ ceramic was prepared using a solid-state reaction method and crystalline in tetragonal structure. Sample has high density and purity, which is confirmed from SEM and EDX analysis. Raman spectrum analysis confirms the vibrational modes of all constituent elements in $BiFeWO_6$ ceramic and supports the purity results from EDX analysis. Raman study confirms the presence of all atomic vibrations whereas UV visible study reveals the material has bandgap energy of 1.41 eV, suitable for photovoltaic application. Dielectric study reveals presence of Maxwell-Wanger type of polarization effect and possesses high dielectric constant and low dielectric loss. Study of impedance plots versus frequency at some selected temperatures confirms the NTCR nature and well-supported from the results of Nyquist plots. Analysis of the ac conductivity versus frequency & temperature reveals the fact that conduction mechanism in the sample is controlled by the thermally activated charge carriers. Again, the calculated values of the activation energy from conductivity study supports semiconducting nature. The study of modulus plots reveals the presence of non-Debye type of relaxation mechanism in the studied sample. Study of resistance versus temperature reveals both NTC and PTC thermistor character. Study of P-E loop reveals the ferroelectric nature of the studied sample and emerges as a promising non-toxic thermistor and ferroelectric applications.

Acknowledgment: The authors would like to thank the host Institute for XRD and SEM-EDX characterization of our sample.

Data availability statement: Data can be supplied on the request.

Conflict of Interest: Authors declare that there is no conflict of interest

References

1. H. Schmid, Multi-ferroic magnetoelectric, Ferroelectric, 162 (1994) 317-338
2. H. Schmid, On ferrotoroidics and electrotoroidic, magnetotoroidic and piezotoroidic effects, Ferroelectric, 252 (2001) 41-50
3. U. S. S. R. I. E. DZYALOSHINSK, Institute for Physical Problems, Academy of Sciences, “ON THE MAGNETO-ELECTRICAL EFFECT IN ANTIFERROMAGNETS,” Jetp, vol. 10, no. 3, pp. 628–629, 1959, [Online]. Available: http://www.jetp.ac.ru/cgi-bin/dn/e_010_03_0628.pdf
4. W. Eerenstein, N. D. Mathur, and J. F. Scott, “Multiferroic and magnetoelectric materials,” Nature, vol. 442, no. 7104, pp. 759–765, 2006, doi: 10.1038/nature05023.
5. G. A. Smolenskii and I. E. Chupis, “Ferroelectromagnets,” Sov. Phys. - Uspekhi, vol. 25, no. 7, pp. 415–448, 1982, doi: 10.1070/PU1982v025n07ABEH004570.
6. Lottermoser and D. Meier, “A short history of multiferroics,” 2020.
7. S. Ghosh, H. Shankar, and P. Kar, “Materials Advances Recent developments of lead-free halide double perovskites : a new superstar in the optoelectronic field,” no. 1, pp. 3742–3765, 2022, doi: 10.1039/d2ma00071g.
8. Ravi Shankar P N and A. Sundaresan, "Synthesis, characterization and multiferroic properties of the doubly-ordered polar perovskite NaLnNiWO6 (Ln = Er, Tm, and Lu)," J. Magn. Magn. Mater., vol. 540, no. August 2021, doi: 10.1016/j.jmmm.2021.168412.

9. H. A. Evans, L. Mao, R. Seshadri, and A. K. Cheetham, “Layered Double Perovskites,” Annu. Rev. Mater. Res., vol. 51, pp. 351–380, 2021, doi: 10.1146/annurev-matsci-092320-102133.
10. L. Boudad, M. Taibi, A. Belayachi, and M. Abd-Lefdil, “Structural, morphological, dielectric and optical properties of double perovskites RBaFeTiO6(R = La, Eu),” RSC Adv., vol. 11, no. 63, pp. 40205–40215, 2021, doi: 10.1039/d1ra06793a.
11. R. Das and R. N. P. Choudhary, “Studies of electrical, magnetic and leakage-current characteristics of double perovskite: Dy2CoMnO6,” J. Alloys Compd., vol. 853, Feb. 2021, doi: 10.1016/j.jallcom.2020.157240.
12. Liangdong Chen, Jie Ding and Xinhua Zhu, A review on research progress of double perovskite oxides for oxygen evolution reaction electrocatalysts and supercapacitors, RSC Appl. Interfaces, 2 (2025) 320-351, DOI: https://doi.org/ 10.1039/d4lf00395k
13. J. B. Neaton, C. Ederer, U. V Waghmare, N. A. Spaldin, and K. M. Rabe, “First-principles study of spontaneous polarization in multiferroic \mathrm{Bi}\mathrm{Fe}{\mathrm{O}}_{3}$,” Phys. Rev. B, vol. 71, no. 1, p. 14113, Jan. 2005, doi: 10.1103/PhysRevB.71.014113.
14. B. B. Van Aken, T. T. M. Palstra, A. Filippetti, and N. A. Spaldin, “The origin of ferroelectricity in magnetoelectric YMnO3.,” Nat. Mater., vol. 3, no. 3, pp. 164–170, Mar. 2004, doi: 10.1038/nmat1080.
15. M. Fiebig, “Revival of the magnetoelectric effect,” vol. 123, 2005, doi: 10.1088/0022-3727/38/8/R01.
16. A. Manbachi and R. S. C. Cobbold, “Review Development and application of piezoelectric materials for ultrasound generation and detection,” pp. 187–196, 2011.
17. A. S. Borovik-romanov, Piezomagnetism in the antiferromagnetic fluorides of cobalt and manganese,” 2015.
18. I. Dzyaloshinsky, “A thermodynamic theory of ‘weak’ ferromagnetism of antiferromagnetics,” J. Phys. Chem. Solids, vol. 4, no. 4, pp. 241–255, 1958,
19. S.-W. C. Shuai Dong Jun-Ming Liu and Z. Ren, “Multiferroic materials and magnetoelectric physics: symmetry, entanglement, excitation, and topology,” Adv. Phys., vol. 64, no. 5–6, pp. 519–626, 2015
20. W. Eerenstein, N. D. Mathur, and J. F. Scott, Multiferroic and magnetoelectric materials., Nature, vol. 442, no. 7104, pp. 759–765, Aug. 2006

21. T. Kimura, T. Goto, H. Shintani, K. Ishizaka, T. Arima, and Y. Tokura, "Magnetic control of ferroelectric polarization," Nature, vol. 426, no. 6962, pp. 55–58, 2003, doi: 10.1038/nature02018.
22. K. Z. Rushchanskii et al., "A multiferroic material to search for the permanent electric dipole moment of the electron," Nat. Mater., vol. 9, no. 8, pp. 649–654, 2010, doi: 10.1038/nmat2799.
23. H. Katsura, N. Nagaosa, and A. V Balatsky, "Spin Current and Magnetoelectric Effect in Noncollinear Magnets," Phys. Rev. Lett., vol. 95, no. 5, p. 57205, Jul. 2005, doi: 10.1103/PhysRevLett.95.057205.
24. H. Palneedi, V. Annapureddy, S. Priya, and J. Ryu, "Status and Perspectives of Multiferroic Magnetoelectric Composite Materials and Applications," Actuators, vol. 5, p. 9, 2016, [Online]. Available: https://api.semanticscholar.org/CorpusID:16174537
25. Z. F. R. K. F. Wang, J. –M. Liu, "Multiferroicity — The coupling between magnetic and polarization orders K.," no. Tadp 392227.
26. N. A. Spaldin and M. Fiebig, "No Title," vol. 391, no. 2005, 2013, doi: 10.1126/science.1113357.
27. R. Palai, H. Schmid, J. F. Scott, and R. S. Katiyar, "Raman spectroscopy of single-domain multiferroic ${\text{BiFeO}}_{3}$," Phys. Rev. B, vol. 81, no. 6, p. 64110, Feb. 2010, doi: 10.1103/PhysRevB.81.064110.
28. J. Wang et al., "Epitaxial BiFeO3 multiferroic thin film heterostructures.," Science, vol. 299, no. 5613, pp. 1719–1722, Mar. 2003, doi: 10.1126/science.1080615.
29. A. Puhan, B. Bhushan, A. K. Nayak, and D. Rout, Chapter 12 - BiFeO3-based multiferroic materials and their properties. Elsevier Inc., 2021. doi: 10.1016/B978-0-12-822352-9.00008-0.
30. K. N. Kumar, S. A. Sattar, G. V. A. Reddy, R. I. Jafri, and R. Premkumar, "Structural, optical, and electrochromic properties of RT and annealed sputtered tungsten trioxide - (WO 3) thin films for electrochromic applications by using the GLAD technique," J. Mater. Sci. Mater. Electron., vol. 34, no. 28, pp. 1–11, 2023, doi: 10.1007/s10854-023-11285-x.
31. P. M. Woodward, A. W. Sleight, and T. Vogt, "Ferroelectric Tungsten Trioxide," IEEE J. Solid-State Circuits, vol. 131, pp. 9–17, 1997, [Online]. Available: https://api.semanticscholar.org/CorpusID:97603688
32. J. Rout, B. N. Parida, P. R. Das, and R. N. P. Choudhary, "Structural, dielectric, and electrical properties of BiFeWO6 ceramic," J. Electron. Mater., vol. 43, no. 3, pp. 732–739, 2014, doi: 10.1007/s11664-013-2923-2.

View Article Online
DOI: 10.1039/D5MA00643K

33. A. Malathi, Prabhakarn Arunachalam, Andrews Nirmala Grace, J. Madhavan, Abdullah M. Al-Mayouf, A robust visible-light driven $BiFeWO_6$/BiOI nanohybrid with efficient photocatalytic and photoelectrochemical performance, Applied Surface Science, 412 (2017) 85-89, https://doi.org/10.1016/j.apsusc.2017.03.199
34. Cong Lu, Yongli Yin, Haifeng Zhou, Construction of oxygen vacancy enriched Bi_2MoO_6/$BiFeWO_6$ heterojunction for efficient degradation of organic pollutants, Journal of Solid State Chemistry, 312 (2022) 123210, https://doi.org/10.1016/j.jssc.2022.123210
35. Alharbi, F.F., Aman, S., Ahmad, N. *et al.* Rational design of a $BiFeWO_6$ nanostructure for supercapacitor applications. J Solid State Electrochem 26, (2022). 1251–1258, https://doi.org/10.1007/s10008-022-05154-6
36. N. Raengthon, C. McCue and D. P. Cann, J. Adv. Dielectr. 6, 1650002 (2016)
37. A. K. Singh, Experimental Methodologies for the Characterization of Nanoparticles. 2016. doi: 10.1016/b978-0-12-801406-6.00004-2.
38. A.B.J. Kharrat, N. Moutia, K. Khirouni, W. Boujelben, Investigation of electrical behavior and dielectric properties in polycrystalline $Pr_{0.8}Sr_{0.2}MnO_3$ manganite perovskite, Mater. Res. Bull. 105, 75-83 (2018)
39. S. Patel, A. Raulji, D. Patel, D. Panchal, M. Dalwadi, and U. Upadhyay, "A Review on 'Uv Visible Spectroscopy,'" Int. J. Pharm. Res. Appl., vol. 7, no. 5, pp. 1144–1151, 2022, [Online]. Available: www.ijprajournal.com
40. Ankita Meher, Amrita Palai, Nihar Ranjan Panda, Satya Prakash Pati & Dojalisa Sahu, Synthesis of zinc oxide/bismuth oxide nanocomposite photocatalyst for visible light-assisted degradation of synthetic dyes and antibacterial application. Environ Sci Pollut Res (2025). https://doi.org/10.1007/s11356-024-35804-3
41. J. Tauc, R. Grigorovici, and A. Vancu, "Optical Properties and Electronic Structure of Amorphous Germanium," Phys. status solidi, vol. 15, no. 2, pp. 627–637, 1966, doi: https://doi.org/10.1002/pssb.19660150224.
42. K. S. Usha, R. Sivakumar, and C. Sanjeeviraja, "Optical constants and dispersion energy parameters of NiO thin films prepared by radio frequency magnetron sputtering technique," J. Appl. Phys., vol. 114, no. 12, 2013, doi: 10.1063/1.4821966.
43. Y. Wang et al., "One-step hydrothermal synthesis of a novel 3D BiFeWOx/Bi2WO6 composite with superior visible-light photocatalytic activity," Green Chem., vol. 20, no. 13, pp. 3014–3023, 2018, doi: 10.1039/c7gc03731g.

44. C. Lu, W. Wu, and H. Zhou, "In situ fabrication of BiOBr/BiFeWO6 heterojunction with excellent photodegradation activity under visible light," J. Solid State Chem., vol. 303, no. July, p. 122465, 2021, doi: 10.1016/j.jssc.2021.122465.
45. A. Priya et al., "Fabrication of visible-light active BiFeWO 6 / ZnO nanocomposites with enhanced photocatalytic activity," Colloids Surfaces A, vol. 586, no. November 2019, p. 124294, 2020, doi: 10.1016/j.colsurfa.2019.124294.
46. J. A. Khan and J. Ahmad, "Double perovskite La 2 CrMnO 6 : synthesis, optical and transport properties Double perovskite La 2 CrMnO 6 : synthesis, optical and transport properties," pp. 0–12, 2019.
47. B. S. Tripathy, R. N. P. Choudhary, and S. K. Parida, "A Double Perovskite BiFeMoO 6 : Microstructural, Optical, Dielectric, and Transport Properties," pp. 1–15, 2023, doi: 10.1142/S201032472350011X.
48. S. K. Tripathy, "Refractive indices of semiconductors from energy gaps," Opt. Mater. (Amst)., vol. 46, pp. 240–246, 2015, doi: 10.1016/j.optmat.2015.04.026.
49. P. Mallick, "Effect of solvent on the microstructure and optical band gap of ZnO nanoparticles," Indian J. Pure Appl. Phys., vol. 55, no. 3, pp. 187–192, 2017.
50. S. Munir, S. M. Shah, H. Hussain, and R. Ali Khan, "Effect of carrier concentration on the optical band gap of TiO2 nanoparticles," Mater. Des., vol. 92, pp. 64–72, 2016, doi: 10.1016/j.matdes.2015.12.022.
51. C. Huang, F. Wang, C. Wu, H. Huang, and C. Yang, "43. NiO-TZO diode transmittance Huang2013_Article_DevelopingHigh-transmittanceHe.pdf," pp. 1–8, 2013
52. M. H. Mamat et al., "Synthesis, structural and optical properties of mesostructured, X-doped NiO (x = Zn, Sn, Fe) nanoflake network films," Mater. Res. Bull., vol. 127, p. 110860, 2020, doi: https://doi.org/10.1016/j.materresbull.2020.110860.
53. G. Malik, J. Jaiswal, S. Mourya, and R. Chandra, "Optical and other physical properties of hydrophobic ZnO thin films prepared by dc magnetron sputtering at room temperature," J. Appl. Phys., vol. 122, no. 14, p. 143105, Oct. 2017, doi: 10.1063/1.5007717.
54. Raman study of the phonon symmetries in BiFeO3 single crystals, C. Beekman, A. A. Reijnders, Y. S. Oh, S. W. Cheong, and K. S. Burch, Phys. Rev. B 86, 020403(R) – Published 18 July 2012, https://doi.org/10.1103/PhysRevB.86.020403.
55. Ferroelastic domain identification in $BiFeO_3$ crystals using Raman spectroscopy, Cameliu Himcinschi, Jan Rix, Christian Röder, Martin Rudolph, Ming-Min Yang, David Rafaja, Jens Kortus & Marin Alexe, Scientific Reports, Nature, Published:2019, DOI:10.1038/s41598-018-36462-5

View Article Online
DOI: 10.1039/D5MA00643K

56. Structural and magnetic properties of isovalently substituted multiferroic BiFeO3: Insights from Raman spectroscopy, Johan Bielecki, Peter Svedlindh, Dessie T. Tibebu, Shengzhen Cai, Sten-G. Eriksson, Lars Börjesson, and Christopher S. Knee, Phys. Rev. B 86, 184422 – Published 19 November 2012, DOI: https://doi.org/10.1103/PhysRevB.86.184422
57. P. Keburis, J. Banys, A. Brilingas, J. Prapuolenis, A. Kholkin, and M. E. V. Costa, "Dielectric properties of relaxor ceramics BBN," Ferroelectrics, vol. 353, no. 1 PART 3, pp. 149–153, 2007, doi: 10.1080/00150190701368109.
58. Nihar Ranjan Panda, Sangran K. Sahu, Amrita Palai, Tarun Yadav , Debadhyan Behera , Dojalisa Sahu, Unraveling the synergistic effects in ZnO-MoS_2 nanocomposite leading to enhanced photocatalytic, antibacterial and dielectric characteristics, Chemical Physics Impact, 8 (2024) 100550, https://doi.org/10.1016/j.chphi.2024.100550
59. Dojalisa Sahu, Nihar Ranjan Panda, Synthesis of novel nanocomposite of g-C_3N_4 coated ZnO–MoS_2 for energy storage and photocatalytic applications, Chemosphere, 350 (2024) 141014, https://doi.org/10.1016/j.chemosphere.2023.141014
60. K. B. R. Varma and K. V. R. Prasad, "Structural and dielectric properties of Bi2NbxVi−xO5.5 ceramics," J. Mater. Res., vol. 11, no. 9, pp. 2288–2292, 1996, doi: 10.1557/JMR.1996.0291.
61. S. Mishra, R.N.P. Choudhary, S. K. Parida; Microstructure, dielectric relaxation, optical, and ferroelectric studies of a lead-free double perovskite: BaLiFeMoO6, J. Korean Ceram. Soc., 60 (2023) 310-330.
62. P. Fischer, M. Polomska, I. Sosnowska, and M. Szymanski, "Temperature dependence of the crystal and magnetic structures of BiFeO 3," J. Phys. C Solid State Phys., vol. 13, no. 10, pp. 1931–1940, Apr. 1980, doi: 10.1088/0022-3719/13/10/012.
63. R. K. Mishra, D. K. Pradhan, R. N. P. Choudhary, and A. Banerjee, "Dipolar and magnetic ordering in Nd-modified BiFeO3 nanoceramics," J. Magn. Magn. Mater., vol. 320, no. 21, pp. 2602–2607, 2008, doi: https://doi.org/10.1016/j.jmmm.2008.05.005.
64. L. Benguigui, "Thermodynamic theory of the morphotropic phase transition tetragonal-rhombohedral in the perovskite ferroelectrics," Solid State Commun., vol. 11, no. 6, pp. 825–828, Sep. 1972, doi: 10.1016/0038-1098(72)90280-3.
65. S. Mishra, R.N.P. Choudhary, S. K. Parida; Structural, Dielectric, Electrical and Optical Properties of Li/Fe Modified Barium Tungstate Double Perovskite for Electronic Devices; Ceram. Int., 48 (2022) 17020-1703.

66. R. J. D. TILLEY, “Correlation between dielectric constant and defect structure of non-stoichiometric solids,” Nature, vol. 269, no. 5625, pp. 229–231, 1977, doi: 10.1038/269229a0.
67. N. Singh, A. Agarwal, S. Sanghi, and P. Singh, “Synthesis, microstructure, dielectric and magnetic properties of Cu substituted Ni–Li ferrites,” J. Magn. Magn. Mater., vol. 323, no. 5, pp. 486–492, Mar. 2011, doi: 10.1016/J.JMMM.2010.09.053.
68. S. Mishra, R. N. P. Choudhary, and S. K. Parida, Structural, dielectric, electrical and optical properties of a double perovskite: BaNaFeWO6 for some device applications, J. Mol. Struct., vol. 1265, p. 133353, Oct. 2022, doi: 10.1016/J.MOLSTRUC.2022.133353.
69. S. K. Parida and R. N. P. Choudhary, Preparation method and cerium dopant effects on the properties of BaMnO3 single perovskite, Phase Transitions, vol. 93, no. 10–11, pp. 981–991, 2020, doi: 10.1080/01411594.2020.1817451.
70. Z.-L. Hou, M.-S. Cao, J. Yuan, X.-Y. Fang, and X.-L. Shi, "High-temperature conductance loss dominated defect level in h-BN: Experiments and first-principles calculations," J. Appl. Phys., vol. 105, no. 7, p. 76103, Apr. 2009, doi: 10.1063/1.3086388.
71. W.-L. Song, M.-S. Cao, Z.-L. Hou, X.-Y. Fang, X.-L. Shi, and J. Yuan, “High dielectric loss and its monotonic dependence of conducting-dominated multiwalled carbon nanotubes/silica nanocomposite on temperature ranging from 373 to 873 K in X-band,” Appl. Phys. Lett., vol. 94, no. 23, p. 233110, Jun. 2009, doi: 10.1063/1.3152764.
72. H. Singh, A. Kumar, and K. L. Yadav, “Structural, dielectric, magnetic, magnetodielectric and impedance spectroscopic studies of multiferroic BiFeO3–BaTiO3 ceramics,” Mater. Sci. Eng. B, vol. 176, no. 7, pp. 540–547, 2011, doi: https://doi.org/10.1016/j.mseb.2011.01.010.
73. V. Provenzano, L. P. Boesch, V. Volterra, C. T. Moynihan, And P. B. Macedo, “Electrical Relaxation in Na2O·3SiO2 Glass,” J. Am. Ceram. Soc., vol. 55, no. 10, pp. 492–496, Oct. 1972, doi: https://doi.org/10.1111/j.1151-2916.1972.tb13413.x.
74. A. K. Jonscher, “The ‘universal’ dielectric response,” Nature, vol. 267, no. 5613, pp. 673–679, 1977, doi: 10.1038/267673a0.
75. Sahoo, S.: Enhanced time response and temperature sensing behavior of thermistor using Zn-doped CaTiO3 nanoparticles. J. Adv. Ceram. 7, 99–108 (2018)
76. Saha, D.; Das Sharma, A.; Sen, A.; Maiti, H.S.: Preparation of bixbyite phase (MnxFe1–x)2O3 for NTC thermistor applications. Mater. Lett. 55, 403–406 (2002)

View Article Online
DOI: 10.1039/D5MA00643K

77. Zhang, S., Malič, B., Li, JF. *et al.* Lead-free ferroelectric materials: Prospective applications. *Journal of Materials Research* **36**, 985–995 (2021). https://doi.org/10.1557/s43578-021-00180-y.
78. (Temperature dependence of the coercive field in single-domain particle systems; W. C. Nunes, W. S. D. Folly, J. P. Sinnecker, and M. A. Novak Phys. Rev. B 70, 014419 – Published 19 July 2004, DOI: https://doi.org/10.1103/PhysRevB.70.014419.
79. Temperature and frequency dependence of the coercive field of $0.71PbMb_{1/3}Nb_{2/3}O_3$–$0.29PbTiO_3$ relaxor-based ferroelectric single crystal; Yang Zhang; Zhaojiang Chen; Wenwu Cao; Zhongwu Zhang; *Appl. Phys. Lett.* 111, 172902 (2017) https://doi.org/10.1063/1.4998187)
80. Yu, H., & Shin, C. (2021). Impact of Rapid-Thermal-Annealing Temperature on the Polarization Characteristics of a PZT-Based Ferroelectric Capacitor. Electronics, 10(11),1324. https://doi.org/10.3390/electronics10111324.

View Article Online
DOI: 10.1039/D5MA00643K

Data Availability Statement: Data will made available on reasonable requestion from the Authors